ACS OMEGA

http://pubs.acs.org/journal/acsodf

Article

Engineering Porous Silicon-Based Microcavity for Chemical Sensing

Ivan Ivanov,* Valeriy Skryshevsky, and Ali Belarouci

Cite This: *ACS Omega* 2023, 8, 21265−21276

Read Online

ACCESS | Metrics & More | Article Recommendations

ABSTRACT: In this article, the authors theoretically and experimentally investigated ways to improve the efficiency of porous silicon (PS)-based optical microcavity sensors as a 1D/2D host matrix for electronic tongue/nose systems. The transfer matrix method was used to compute reflectance spectra of structures with different $[n_L\ n_H]$ sets of low n_L and high n_H bilayer refractive indexes, the cavity position λ_c, and the number of bilayers N_{bi}. Sensor structures were prepared by electrochemically etching a silicon wafer. The kinetics of adsorption/desorption processes of ethanol−water-based solution was monitored in real time with a reflectivity probe-based setup. It was theoretically and experimentally demonstrated that the sensitivity of the microcavity sensor is higher for structures with refractive indexes in the lower range (and the corresponding porosity values in the upper range). The sensitivity is also improved for structures with the optical cavity mode (λ_c) adjusted toward longer wavelengths. The sensitivity of a distributed Bragg reflector (DBR) with cavity increases for a structure with cavity position λ_c in the long wavelength region. The full width at half maximum ($fwhm_c$) of the microcavity is smaller and the quality factor of microcavity (Q_c) is higher for the DBR with a larger number of structure layers N_{bi}. The experimental results are in good agreement with the simulated data. We believe that our results can help in developing rapid, sensitive, and reversible electronic tongue/nose sensing devices based on a PS host matrix.

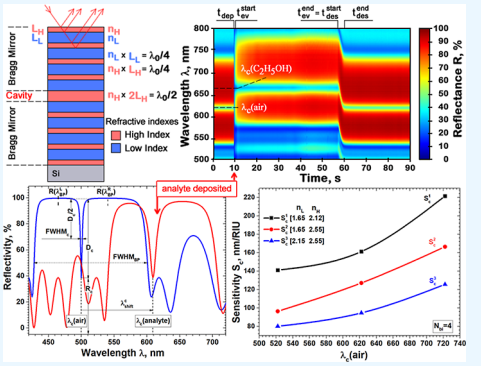

1. INTRODUCTION

The rapid increase in human population and consumption, the development of new territories for agriculture, the buildup of industries, and the elevated pressure from pandemics in the world call for rapid progress in monitoring devices to control the pollution of the environment, use of medicines, quality of products of consumption, medical safety, and presence of toxic, explosive, and drug substances. These global challenges require cheap but efficient sensors and sensor systems, mass production of low-cost technologies, and materials in both industrialized and developing countries.

One of the promising materials for sensing applications is porous silicon (PS).[1] PS has a sponge-like structure with a high surface-to-volume ratio.[2] Adsorption of analyte molecules on pore walls changes the optical and electrical properties of PS used for sensor applications.[3] The cheap and technologically simple process of electrochemical anodization[4] allows us to control the morphology, size, and distribution of pores that authorize fabricating both single-layer- and multilayer-based sensor structures.[5] Optical, electrical, and impedance methods[6] are widely used for the characterization of PS sensors. Optical methods, such as fast methods of sensor response detection, have been mainly used for multilayer structures like Fabry−Perot filters,[7] Bragg reflectors,[8] optical microcavities,[9] and surface gratings.[10,11]

Photonic crystals (PCs) are periodic dielectric nanomaterials affecting the propagation characteristics of light.[12] The propagation of certain wavelengths of light is forbidden in these artificial materials due to the photonic band gaps (PBGs) that originate from the periodic modulation of the dielectric medium. Although many efforts have been paid to design and develop ordered two- and three-dimensional structures, one-dimensional (1D) PCs, also known as Bragg mirrors (BMs), consisting of layered alternating materials with different refractive indices along one direction, have attracted great attention because of their simple structure, high reflectivity, convenient fabrication process, and relatively easy prediction of their optical properties. Bright and high-saturation color appears when the PBG is located in the visible region, which makes these structures good candidates for applications such as highly efficient reflectors,[13] chemical/physical sensors,[14,15] and dynamic color displays.[16] When combined with porous materials, 1D PCs have unique optical properties that can be exploited to engineer smart devices. The optical properties of PS PBG devices are extremely sensitive to small changes of refractive index in the porous layers.[17] Therefore, adsorption of analyte molecules within the structure alters the effective

Received: April 13, 2023
Accepted: May 19, 2023
Published: June 1, 2023

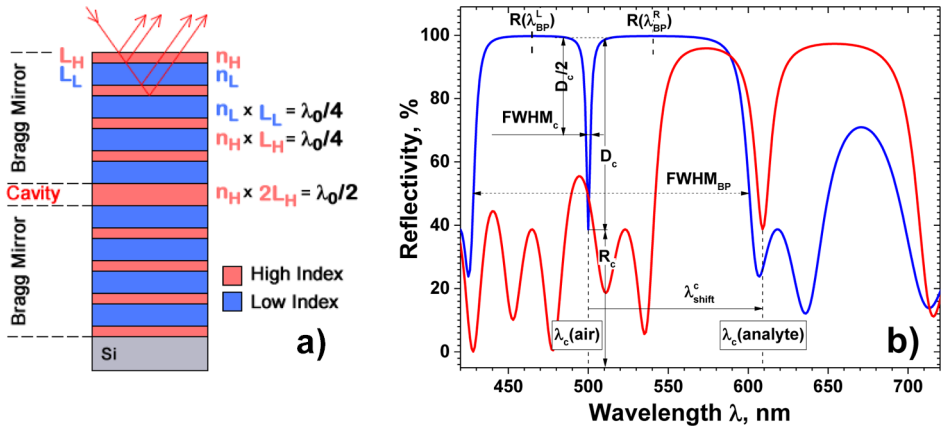

Figure 1. (a) Schematic refractive index profile of the microcavity and (b) dependence of the reflectance spectra of the microcavity calculated for pores filled with air and ethanol (λ_0(air) = 500 nm, $N_{bilayer}$ = 4, n_H = 2.44, n_L = 1.54, construction $(n_H n_L)^{N_{bi\text{-}layer}} n_H (n_L n_H)^{N_{bi\text{-}layer}} n_{Si}$).

refractive index, thus affecting the distributed Bragg reflector (DBR) sensor parameters such as the spectral position, intensity, and width of the PBGs.[18]

PS microcavities, on the other hand, provide the opportunity to sharpen the broad spectral response of DBRs. The geometrical structure of the microcavity consists of two parallel mirrors separated by a spacer layer with an optical thickness of λ or $\lambda/2$[19] to display a single photon mode. The reflectivity spectrum is defined as a narrow transmission line centered between two highly reflecting bands. Microcavities can be exploited to enhance and amplify fluorescence or luminescence,[20] filter and narrow the emission signal of both the porous matrix and implanted nanoparticles, and as a result reduce the analyte volume and analysis time.[21] To further increase the sensitivity and detectability, complex refractive index profiles have been engineered. For instance, several anodization schemes of refractive index profiles are used to decrease the effect of side interference peaks.[22]

An optical porous sensor is made of a transducer component and a chemical or biological recognition element. The transducer transforms each physical, chemical, or biochemical interaction into an optical signal that finally will be converted into electrical form for further analog and digital processing. When molecules are adsorbed on the internal pore walls of the PS microcavity, a change in the reflectivity/transmission spectrum is observed. The adsorption of molecules induces an increase in the average refractive index of the layers, thereby shifting the spectral response toward longer wavelengths. There is a linear relationship between the red shift of the interference peaks and the reflective index of the analyte.[23] Chemical (functional groups) or biological recognition elements (DNA single strands, enzymes, proteins,[24] antibodies, antigens, etc.[25]) are coupled with the transducer matrix. While the design and fabrication of the porous Si-based PBG transducer establishes the main sensor sensitivity, the chemical or bio-functionalization is considered a recognition element of the sensor and defines the analyte selectivity.[26,27] The response of a PS-based microcavity can be recorded at the end of transient processes (steady-state mode) or monitored in real-time before, during, and after exposure (dynamic mode) to investigate the kinetics of adsorption/desorption processes.[28]

Porous Si-based microcavities are promising for the fabrication of complex sensor systems such as the electronic tongue[29] and electronic nose.[30,31] They can also be included in a multisensory system[32,33] that generally consists of a 1D/2D/3D array of separate sensors or a multiparametric system on a single chip[34] with coordinate dependence of sensor parameters.[35,36] Electronic tongue/nose systems are used for the classification of clinical and food samples.[32,33] The complex N-dimensional sensor response[37] is considered as a pattern of smell or taste and processed with pattern recognition systems with artificial neural networks.[38] In recent years, the studies of porous sensor structures to detect viruses[35,39,40] and bacteria[41,42] have been actively conducted and the development of electronic tongue/nose sensor systems is propitious for this field of applications.

The novelty of this article consists of comprehensive analysis of a 1D PC sensor based on PS with a microcavity to explore ways to increase the sensitivity of the sensor while ensuring the detectability of the microcavity as the primary feature of the spectral response of the sensor is not compromised. The optical sensing structure with parameter λ_c and/or $[n_L\ n_H]$ along one or two axes of the device can be considered as an electronic tongue/nose with a response-forming analyte-specific pattern that could be used for recognition with neural network-based machine learning systems. The time dependence of the analyte response pattern is envisioned as a way to improve sensor recognition and selectivity. The suggested methods provide a route to fabricate the porous microcavity as an effective universal optical transducer that can be chemically or biochemically functionalized for a specific analyte. PS possesses several advantages that make it an excellent material for manufacturing optical sensors. First, it enables the fabrication of porous PCs, utilizing inexpensive electrochemical etching technology. Second, it is compatible with the existing silicon technology, making it an attractive choice for developing optical sensor structures that can operate both independently and as a host for immobilizing chemical or biological recognition elements. Thus, PS offers a highly versatile and cost-effective platform for developing optical sensors with various functionalities.

The objective of motivation for this work is to propose a comprehensive study of the PS-based microcavity structure as a basic transducer before the next chemical and biochemical functionalization for the purpose of increasing the sensitivity and detectability of the sensor response. Section 2 describes the design and results of simulation of the structure for a wide range of parameters. Section 3 highlights the fabrication process and the experimental setup developed to control, in real-time, the modification of the spectral response of the PBG

https://doi.org/10.1021/acsomega.3c02526
ACS Omega 2023, 8, 21265−21276

sensing device. Finally, in Section 4, the experimental results are reported and discussed.

2. SAMPLES AND SIMULATION OF REFLECTANCE SPECTRA

2.1. Design of the Photonic Structure. The optical microcavity is made of a pair of symmetrical multilayer BMs, separated by a spacer or "defect" layer (Figure 1a). The BM is a sequence of alternative layers with high (n_H) and low (n_L) refractive indexes. The optical thickness of each BM layer satisfies the relation $n_H \times L_H = n_L \times L_L = \lambda_0/4$, where L_H and L_L are the physical thicknesses of layers with high and low refractive indexes, respectively, and λ_0 is the position of the reflectance extremum. The constructive interference of the reflected wavelengths produces a forbidden optical band which is materialized by a high reflectance spectral region named Bragg peak (BP).

The presence of a "defect" layer (optical thickness $n_S \times L_S \neq \lambda_0/4$) within the DBR modifies drastically the optical response by introducing a level of transmission inside the forbidden gap. For a PB structure with a spacer of optical thickness $\lambda_0/2$, there is destructive interference of reflected light around λ_0 that forms the allowed optical band as a cavity at $\lambda_0 = \lambda_c$ on the reflectance spectrum. The optical microcavity is described by the refractive index profile $(n_H n_L)^{N_{bi\text{-}layer}} n_H (n_L n_H)^{N_{bi\text{-}layer}} n_{Si}$), where $N_{bilayer}$ is the number of BM bilayers (n_H n_L) and n_{Si} is the refractive index of the silicon wafer. The "defect" layer thickness fulfills the relation $n_S \times L_S = n_H \times 2L_H = \lambda_0/2$. The reflectance spectrum of the microcavity displays a narrow optical mode inside the stop band. The penetration of analyte molecules inside the pores of the microcavity increases the effective refractive index of each layer and gives rise to a red shift of the reflectance spectra. While the shift for a DBR can be difficult to estimate, in particular for a highly reflective stop band, non-symmetrical and noisy response and the presence of a sharp optical transmission mode inside the PBG for a microcavity make it more easy to track precisely the shift induced by adsorption of species.

The spectral response of the sensor is described by the position of cavity λ_c, the reflectance R_c at λ_c, the level of transmission of the cavity mode D_c, and the cavity full width at half maximum ($fwhm_c$). The sensitivity of the sensor is determined by the change of parameter λ_c. Parameters D_c, R_c, and $fwhm_c$ drive the detectability of the cavity. The minimum detectable $fwhm_c$ is limited by the spectral resolution of the spectrometer/monochromator, and its value strongly depends on the quality of the interface between layers.[1] Parameters D_c and R_c define the detectability of the cavity on the background of side interference fringes and noisiness of the spectrum. Filling of pores with analyte generates a shift of the cavity mode position from $\lambda_c(n_{air}) = \lambda_c(air) = \lambda_c^{min}$ to $\lambda_c(n_{analyte}) = \lambda_c(analyte) = \lambda_c^{max}$, and this wavelength range can be considered as the sensor wavelength working range $\lambda_c^{min}...\lambda_c^{max}$. The cavity divides the host BP into left λ_{DBR}^L and right λ_{DBR}^R sub-peaks with a maxima of reflectance $R_{DBR}^L = R(\lambda_{DBR}^L)$ and $R_{DBR}^R = R(\lambda_{DBR}^R)$, respectively, for the left and right sub-peaks. In general, these sub-peaks can be asymmetrical: $R_{DBR}^L \neq R_{DBR}^R$ and $fwhm_{DBR}^L \neq fwhm_{DBR}^R$. The detectability of the cavity mode is higher for DBR with flat and high reflectivity BP in the wavelength range $\lambda_{min}^s = \lambda_{min}^c - fwhm_{DBR}^L(air)...\lambda_{max}^c + fwhm_{DBR}^R(analyte) = \lambda_{max}^s$. Parameters of cavity and host BP depend on the refractive indexes of bilayers [n_L n_H] and the number of bilayers $N_{bilayer}$. A high-quality factor microcavity is preferable for sensing applications to precisely assess the cavity mode position λ_c. The fwhm of DBR with a cavity is higher compared to the fwhm of the DBR with the same total $N_{bilayer}$ and, therefore, such structures can be used as rear solar cell reflectors to increase the adsorption length of low-energy photons.

2.2. Simulation of Reflectance Spectra. The reflectance spectra $S(\lambda)$ were computed using the transfer matrix method.[43,44] Bruggeman approximation for the effective medium was used to link the porosity P and the refractive indexes of the DBR with pores filled with air and analyte.[4] Simulations were performed for two nanocomposites (silicon-air and silicon-analyte). Pores were considered as completely filled with the analyte. Fresh fabricated microcavities without any surface modification and functionalization were modeled with the following refractive index profile $(n_H n_L)^{N_{bi\text{-}layer}} n_H (n_L n_H)^{N_{bi\text{-}layer}} n_{Si}$. Spectral dependences were calculated for a wide range of analyte refractive indexes $n_{analyte}$, different sets [n_L n_H] of bilayers, number of bilayers $N_{bilayer}$, and for 8 fixed values of $\lambda_c(air)$. All spectra were simulated in the range $\lambda_{min}...\lambda_{max}$. Parameters range and steps used for simulation are summarized at Table 1. The physical layer thicknesses of the DBR were chosen to satisfy the condition $n_H(air) \times L_H = n_L(air) \times L_L = \lambda_0(air)/4$ with $n_H(air) > n_L(air)$ for all considered pairs [n_L n_H]. The spacer thickness follows the relation $n_H \times 2L_H = \lambda_0$.

Table 1. Parameters, Ranges, and Steps Used for Spectrum Computation of the Microcavities

parameter	range	step
refractive index n_H, n_L ($n_H > n_L$)	$n(air) = n_{min}...n_{max} = n(Si)$	0.02
refractive index of analyte $n_{analyte}$ that fills pores	1.3...1.4	0.001
cavity position $\lambda_0(air)$, nm	400...800	50
wavelength range, nm	$\lambda_{max}^{spec} = 350...\lambda_{max}^{spec} = 1200$	1

The parameters of the microcavity for pores filled with air or analyte were determined from computed spectra: cavity position λ_c, level of transmission of the optical mode $D_c(\lambda_c)$, cavity reflectance $R_c(\lambda_c)$, $fwhm_c$, and parameters of host BP: $fwhm_{DBR}$, R_{DBR}^L, R_{DBR}^R.

The efficiency and performance of the sensor were then evaluated using the following expressions

$$S_{\lambda_c} = \frac{\lambda_c(\text{analyte B}) - \lambda_c(\text{analyte A})}{n(\text{analyte B}) - n(\text{analyte A})} = \frac{\Delta\lambda_c(\text{analyte B} - \text{analyte A})}{\Delta n(\text{analyte B} - \text{analyte A})} \quad (1a)$$

$$S_{R_c} = \frac{R(\lambda_c(\text{analyte B})) - R(\lambda_c(\text{analyte A}))}{n(\text{analyte B}) - n(\text{analyte A})} = \frac{\Delta R_{\lambda_c}(\text{analyte B} - \text{analyte A})}{\Delta n(\text{analyte B} - \text{analyte A})} \quad (1b)$$

$$S_{D_c} = \frac{D(\lambda_c(\text{analyte B})) - D(\lambda_c(\text{analyte A}))}{n(\text{analyte B}) - n(\text{analyte A})} = \frac{\Delta D_{\lambda_c}(\text{analyte B} - \text{analyte A})}{\Delta n(\text{analyte B} - \text{analyte A})} \quad (1c)$$

https://doi.org/10.1021/acsomega.3c02526
ACS Omega 2023, 8, 21265−21276

$$S_{\text{fwhm}_c} = \frac{\text{fwhm}_c(\text{analyte B}) - \text{fwhm}_c(\text{analyte A})}{n(\text{analyte B}) - n(\text{analyte A})} = \frac{\Delta\text{fwhm}_c(\text{analyte B} - \text{analyte A})}{\Delta n(\text{analyte B} - \text{analyte A})} \quad (1d)$$

2.3. Analysis of Microcavity Mode Dependence and Sensitivity. The computed dependence of the mode shift $\Delta\lambda_c(n_{\text{analyte}} = 1.5) = \lambda_c(n_{\text{analyte}} = 1.5) - \lambda_c(\text{air})$ on refractive index n_L and n_H after complete filling of pores with $n_{\text{analyte}} = 1.5$ analyte is depicted in Figure 2 for a microcavity designed at

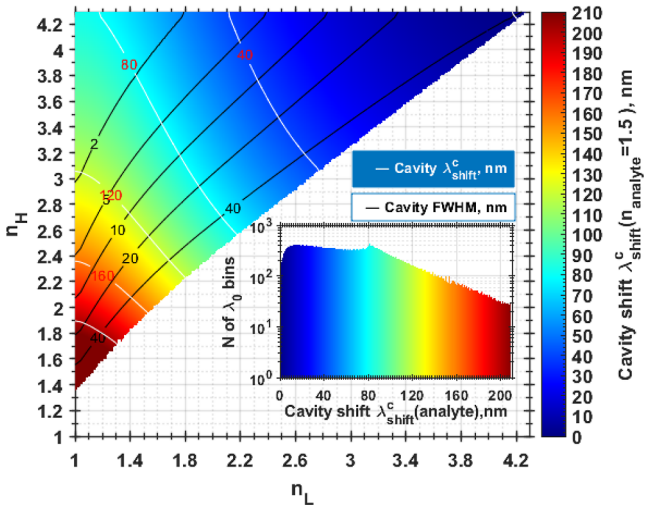

Figure 2. Dependence of the mode shift $\lambda^c_{\text{shift}} = \lambda_c(n_{\text{analyte}} = 1.5) - \lambda_c(n_{\text{air}})$ on refractive indexes n_H and n_L for a microcavity filled with $n_{\text{analyte}} = 1.5$ analyte and air ($\lambda_c(\text{air}) = 600$ nm, $N_{\text{bilayer}} = 4$). The inset corresponds to the histogram of the number of λ^c_{shift} bins with a quantization step of 0.1 nm. White lines depict $\lambda^c_{\text{shift}} = f(n_H, n_L)$ isolines for pores filled with analyte ($n_{\text{analyte}} = 1.5$). Black lines represent $\text{fwhm}_c = f(n_L, n_H)$ isolines for pores filled with analyte ($n_{\text{analyte}} = 1.5$).

$\lambda_c(\text{air}) = 600$ nm and $N_{\text{bilayer}} = 4$. The inset in Figure 2 highlights the histogram of the number of $\Delta\lambda_c$ bins with a 0.1 nm resolution step. The height of the bin bars displays the number of elements in the bin. The shift is in the range 0...210 = $\Delta\lambda_c^{\max}$ and depends on the difference $n_H - n_L$ and their absolute values. The shift $\Delta\lambda_c(\text{analyte})$ and the sensitivity $S_{\lambda_c}(\text{analyte})$ reach, respectively, $\Delta\lambda_c^{\max}(\text{analyte})$ and $S_{S_{\lambda_c}}^{\max}(\text{analyte}) = 420$ nm/RIU when the absolute values n_L and n_H approach $n_{\min} = n(\text{air})$. Sensitivity $S_{\lambda_c}(\text{analyte})$ is higher for DBR with smaller difference $n_H - n_L$, where $[n_L \to n_H = \text{const}]$ or $[n_L = \text{const}\ n_H \to n_L]$.

The sensitivity is larger for structures with higher porous layers (low refractive indexes of layers) due to a larger increase of optical thickness $L_L \times n_L(n_{\text{analyte}})$ and $L_H \times n_H(n_{\text{analyte}})$ compared to structures with low porous layers. The lower limit of refractive indexes n_L and n_H is given by the process and conditions of synthesis. The dependences of $\Delta\lambda_c(n_{\text{analyte}} = 1.5)$ on refractive indexes n_L and n_H were also computed for different designed microcavities ($\lambda_c^i(\text{air}) = 400, 450, 500, 550, 600, 650, 700, 750, 800$ nm).

2.4. Analysis of Cavity Mode fwhm Dependence and Sensitivity. Both the absolute values of refractive indexes $[n_L\ n_H]$ and the difference $n_H - n_L$ define the sensitivity of the microresonator. The precision to estimate the mode position λ_c and the sensitivity S_{λ_c} is higher for a higher quality factor with a smaller fwhm_c (Figure 1b) and cavity with a clear detectable one-point minimum. Determination of sensitivity is complicated for a cavity with a flat bottom or local interference peaks inside the cavity. The computed dependence of mode cavity fwhm_c and its broadening $\Delta\text{fwhm}_c(n_{\text{analyte}} = 1.5) = \text{fwhm}_c(n_{\text{analyte}} = 1.5) - \text{fwhm}_c(\text{air})$ on refractive index n_L and n_H after complete filling of pores with $n_{\text{analyte}} = 1.5$ analyte is depicted in Figure 3 for a microcavity set with $\lambda_c(\text{air}) = 600$ nm and $N_{\text{bilayer}} = 4$.

The analysis of Figure 3a shows that fwhm_c is smaller for structures with a larger $n_H - n_L$ difference. For two DBRs with the same difference $n_H^{\text{DBR1}} - n_L^{\text{DBR1}} = n_H^{\text{DBR2}} - n_L^{\text{DBR2}}$, the cavity mode fwhm_c will be larger for DBRs with smaller absolute values $[n_L\ n_H]$. There are sets $[n_L\ n_H]$ for which the fwhm_c values of the microcavities are small and the accuracy of the determination of microcavity shape and parameters depends on the parameters of the used spectral measurement device. For example, the black color isoline with $\text{fwhm}_c = 3$ nm (Figure 3a) outlines the $[n_L\ n_H]$ region where $\text{fwhm}_c \lesssim 3$. Penetration of analyte molecules into pores causes an increase of the fwhm_c (Figure 3b) and can reach 35 nm for $\lambda_c(\text{air}) = 600$ nm, $N_{\text{bilayer}} = 4$, and $n_{\text{analyte}} = 1.5$ compared to the reference fwhm_c (n_{air}). Therefore, the mode broadening upon adsorption of molecules should be considered when designing the final structure.

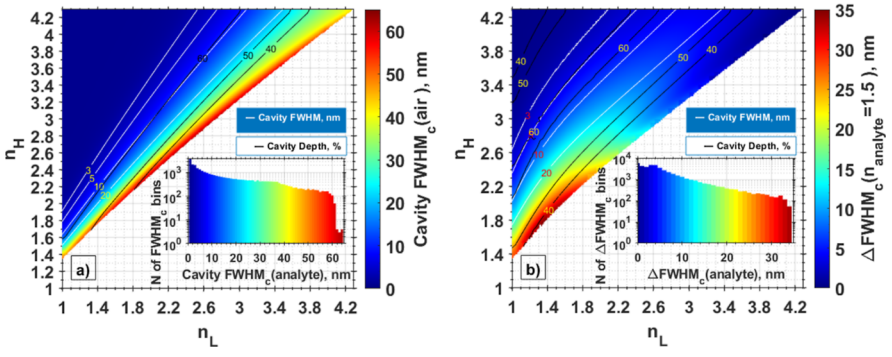

Figure 3. (a) Mapping of the cavity mode fwhm_c versus refractive indexes n_L and n_H for a microcavity designed at $\lambda_0(\text{air}) = 600$ nm filled with analyte ($n_{\text{analyte}} = 1.5$). The inset represents the histogram of the fwhm_c bin numbers with a uniform width of $\text{fwhm}_c = 0.1$ nm and (b) broadening of $\Delta\text{fwhm}_c = \text{fwhm}_c(n_{\text{analyte}} = 1.5) - \text{fwhm}_c(\text{air})$ with refractive indexes n_L and n_H for the same microcavity filled with analyte ($n_{\text{analyte}} = 1.5$) and air. The inset corresponds to the histogram of Δfwhm_c bin numbers with a quantization step of 0.1 nm.

https://doi.org/10.1021/acsomega.3c02526
ACS Omega 2023, 8, 21265−21276

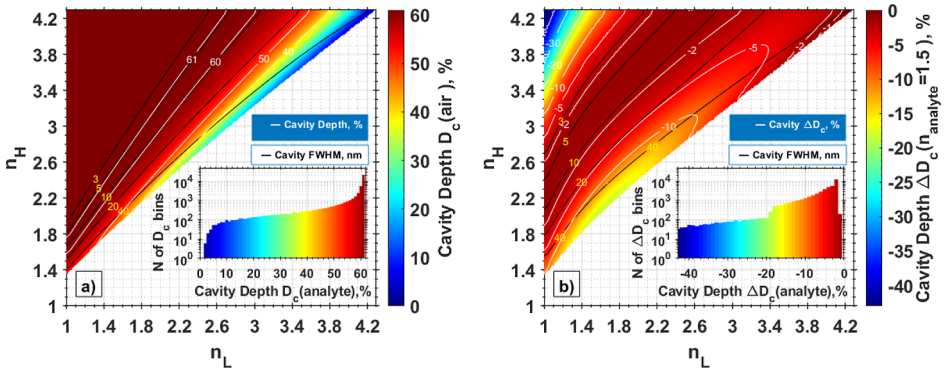

Figure 4. (a) Mapping of the cavity depth D_c versus refractive indexes n_L and n_H for a microcavity designed at λ_c(air) = 600 nm. The inset represents the histogram of the D_c bin numbers with a uniform width of D_c = 0.1% and (b) changing of $\Delta D_c = D_c(n_{analyte} = 1.5) - D_c$(air) with refractive indexes n_L and n_H for the same structure filled with analyte ($n_{analyte}$ = 1.5) and air. The inset corresponds to the histogram of ΔD_c bin numbers with a quantization step of 0.1%.

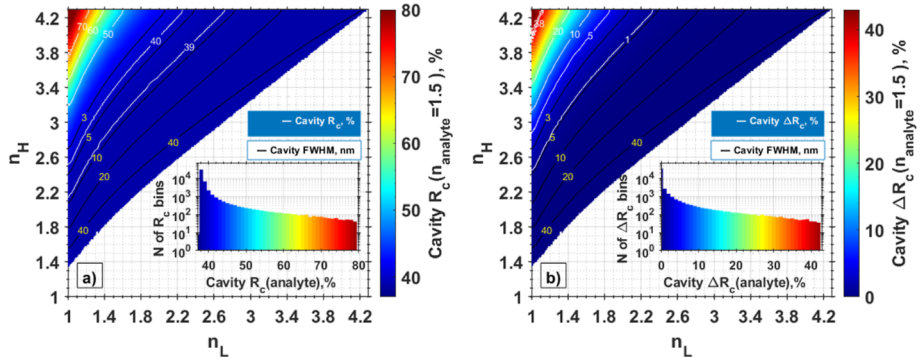

Figure 5. (a) Mapping of the cavity reflection R_c versus refractive indexes n_L and n_H for a microcavity filled with analyte ($n_{analyte}$ = 1.5) and design at λ_c(air) = 600 nm. The inset represents the histogram of the R_c bin numbers with a uniform reflection of R_c = 0.1% and (b) changing of $\Delta R_c = R_c(n_{analyte} = 1.5) - R_c$(air) with refractive indexes n_L and n_H for the same microcavity filled with analyte ($n_{analyte}$ = 1.5) and air. The inset corresponds to the histogram of ΔR_c bin numbers with a quantization step of 0.1%.

2.5. Dependence of Cavity Depth. The parameters of cavity depth D_c depend on $[n_L\ n_H]$, $N_{bilayer}$, and λ_c. The cavity depth influences directly the accuracy to assess λ_c(analyte). A mode cavity with a higher transmission depth is easier to detect within the stop band despite the presence of side interference peaks. This is an important consideration in systems for automatic tracking of cavity mode position. The cavity splits host BP into left and right sub-BP (BP_L, BP_R) with maximum reflectivities $R(\lambda^L_{BP})$ and $R(\lambda^R_{BP})$ at λ^L_{BP} and λ^R_{BP}, respectively (Figure 1b). For an asymmetrical host BP with $R(\lambda^R_{BP}) \neq R(\lambda^R_{BP})$, the base line for cavity depth D_c determination is defined as $(R(\lambda^R_{BP}) + R(\lambda^R_{BP}))/2$.

There is a wide range of $[n_L\ n_H]$ parameters for which D_c = const = 60% (Figure 4a) and is independent of $[n_L\ n_H]$. For microcavities with $[n_L \rightarrow n_H \rightarrow n_L]$, the cavity depth D_c decreases. Penetration of analytes with $n_{analyte}$ = 1.5 into pores induces a maximum decrease of ΔD_c to −44%. The maximum ΔD_c is −15% for the fabricated, in the article, structure $[n^{min}_L$ = 1.5 n^{max}_H = 2.55] with maximum difference $n^{max}_H - n^{min}_H$ that could be obtained for the chosen type of wafer and technological process.

2.6. Dependence of Cavity R. The absolute reflectance R_c at λ_c(analyte) is the parameter that can be directly collected with a detector (Figure 1b). For highly reflective DBR: $R(\lambda^L_{BP})$ = $R(\lambda^R_{BP})$ = 100%, there is the equality R_c (analyte) + D_c (analyte) = 100%. For other configurations, $D_c = (R(\lambda^L_{BP}) + R(\lambda^R_{BP}))/2 - R_c$. The absolute reflectance of the mode $R_c(n_{analyte} = 1.5)$ and $\Delta R_c = R_c(n_{analyte} = 1.5) - R_c(n_{air})$ are almost independent of $[n_L\ n_H]$ in the range n^{min}_L = 1.5...n^{max}_H = 2.55 and increase for $[n_L \rightarrow n^{min}_L\ n_H \rightarrow n^{max}_H]$ (Figure 5a,b, respectively). Increasing of $n_H - n_L$ causes a decrease of the $fwhm_c$. However, there are $[n_L\ n_H]_{max}$ sets for which the accuracy to determine the microcavity parameters is limited by the spectral resolution of the spectrophotometer and can result in an increase of R_c. Discrete step of wavelength (Table 1) in the simulation of reflection spectra of the microcavity also imposes restrictions on the precision of determining the shape and parameters of the cavity mode.

2.7. Dependence of BP $fwhm_{BP}$. The microcavity with $R_c(\lambda_0)$ is determined against the flat top of the host peak consisting of two sub-peaks $R^L_{DBR} > R_c$ and $R^R_{DBR} > R_c$(Figure 1b). The detectability of the mode is higher for a wider stop band (larger $fwhm_{BP}$) due to the increased spatial separation of the mode from the near side interference peaks, which is important in computer recognition of the mode and its parameters. The microresonator has a larger $fwhm_{BP}$ compared to the same structure without a defect-layer DBR.[45] Values of $fwhm_{BP}$ lie in the range 100...700 nm for DBR with λ_c(air) = 600 nm and $N_{bilayer}$ = 4 (Figure 6a). Increasing the difference $n_H - n_L$ leads to the increase of the $fwhm_{BP}$ and the $fwhm_c$ but simultaneously a decrease of the DBR sensitivity (Figure 2b).

2.8. Dependence of Cavity fwhm on the Number of Bilayers $N_{bilayers}$. The dependence of the DBR cavity $fwhm_c$ ($n_{analyte}$) on the number of bilayers $N_{bilayers} = N_{bi}$ for a structure

https://doi.org/10.1021/acsomega.3c02526
ACS Omega 2023, 8, 21265−21276

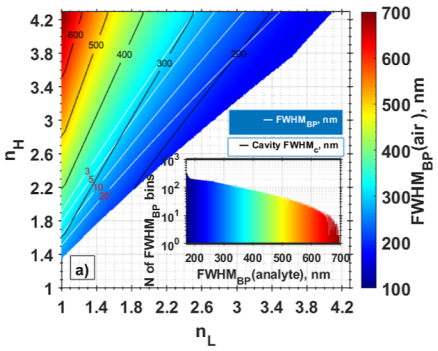

Figure 6. (a) Mapping of the BP fwhm$_{BP}$ versus refractive indexes n_L and n_H for a microcavity designed at λ_c(air) = 600 nm and filled with air (n_{air}). The inset represents the histogram of the fwhm$_{BP}$ bin numbers with a uniform reflection of fwhm$_{BP}$ = 0.1 nm.

with the profile $(n_H n_L)^{N_{bi\text{-}layer}} n_H (n_L n_H)^{N_{bi\text{-}layer}} n_{Si}$ was simulated for microresonators with $[n_L = 1.6\ n_H = 2.3]$ and cavity positions λ_c(air) = 500, 550, 600, 650, 700, 750, 800 nm (Figure 7). Analytes with minimum $n_{analyte} = n_{air} = 1$ and

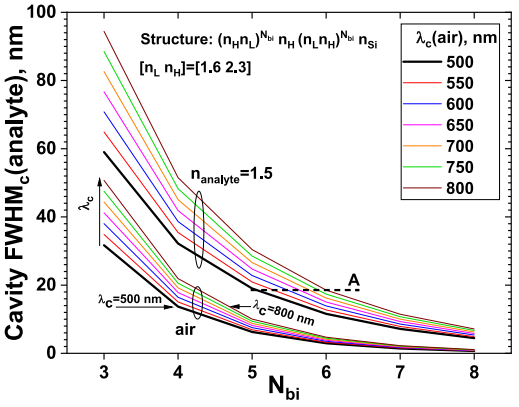

Figure 7. Dependence of the mode cavity fwhm$_c$ ($n_{analyte}$) on number of bilayers N$_{bilayers}$ for DBR cavity positions λ_c(air) = 500, 550, 600, 650, 700, 750, 800 nm for pores filled with air and analyte with $n_{analyte}$ = 1.5. Refractive indexes of layers are $[n_L = 1.6\ n_H = 2.3]$.

maximum $n_{analyte}$ = 1.5 refractive indexes were used to compute spectral dependencies. The fwhm$_c$ decreases with increasing number of $N_{bilayers}$. The fwhm$_c$ of microcavities designed with a cavity mode λ_c in the "red" spectral region is larger compared to structures with λ_c in the "blue" spectral region.

For $N_{bilayers}$ = 5, the difference fwhm$_c$ (λ_c = 800 nm) − fwhm$_c$ (λ_c = 500 nm) = 3.9 nm decreases with increasing $N_{bilayers}$. The increase of the fwhm$_c$ for microcavities designed at longer wavelength regions can be compensated by increasing the number of bilayers. The dashed line A depicts that fwhm$_c$ (λ_c = 500 nm, $N_{bilayers}$ = 5) ≃ fwhm$_c$ (λ_c = 800 nm, $N_{bilayers}$ = 6) for pores filled with analyte ($n_{analyte}$ = 1.5).

3. FABRICATION PROCESS AND EXPERIMENTAL SETUP

3.1. Fabrication Process. 27 microcavities were fabricated with refractive index profiles $(n_H n_L)^{N_{bi\text{-}layer}} n_H (n_L n_H)^{N_{bi\text{-}layer}} n_{Si}$ for different λ_c, $N_{bilayer}$, and sets $[n_L\ n_H]$ depicted in Table 2. Monolithic PSi microcavities were prepared by electrochemical anodization of highly doped p-type c-Si wafers (boron-doped, orientation <100>, resistivity ∼15 mΩ·cm) in a mixed solution of HF acid (35%) and ethanol. The roughness between the layers alters the spectral response of the Fabry−Perot cavity, and the enhancement of light scattering at interfaces induces a low reflectance value. Therefore, the electrolyte temperature was maintained at −40 °C to decrease the etching rate and achieve a high repeatability for the duration of the reaction in order to reduce the roughness of the surface interface. Also, the application of an etch-stop etching method[1] increased the homogeneity of the electrolyte and, as a result, the homogeneity of porosity of each layer. A computer-driven electrical current source Keithley 2401 was used to build a "step"-like current profile to modulate in depth the refractive index profile of the microresonators, so precise control over electrical current and etching time was achieved. The microcavities consisted of a low porosity half-wavelength defect sandwiched between two DBRs made of a series of quarter-wavelength high/low porosity bilayers. The values of single-layer porosities and thicknesses were estimated from the fitting of reflectance spectra in the range of 200−1100 nm and SEM thickness measurements. These estimated values allow the design of 1D PSi PCs, which were experimentally obtained by alternating the two different current densities during the anodization process. Samples were finally rinsed several times with ethanol and dried under nitrogen flow.

Scanning electron microscopy photo of the DBR profile (λ_c = 722 nm, $N_{bilayer}$ = 4, $[n_L\ n_H] = [1.65\ 2.55]$) is depicted in Figure 8a. The cavity widths $L_c = 2L_H$ were determined from SEM images and are depicted in Table 3. The obtained parameters of the layers correspond to the designed parameters due to etching at an electrolyte temperature of −40 °C, which made it possible to reduce the etching rate and, as a result, accurately control the thickness of the layers.

3.2. Experimental Setup. Experimental reflectance spectra were obtained using the setup depicted in Figure 8b. A light source (Thorlabs OSL2) with a 150 W halogen lamp was used to illuminate samples through a reflection bundle fiber RP20 (fiber core diameter: 200 mm). Reflected spectra were acquired with a Thorlabs CCS200 charge-coupled device (CCD)-based spectrometer (wavelength range 200−1000 nm, integration time 10 μs to 60 s, 200 scans/s). A volume of 4 mL of ethanol was deposited on the sample surface using an

Table 2. Parameters of Fabricated Porous DBRs

		N$_{bi\text{-}layer}$		
		4	6	8
λ$_c$, nm	622	[n$_L$ n$_H$] =[1.65 2.12]		
	722	[n$_L$ n$_H$] = [1.65 2.55]		
	822	[n$_L$ n$_H$] = [2.12 2.55]		

https://doi.org/10.1021/acsomega.3c02526
ACS Omega 2023, 8, 21265−21276

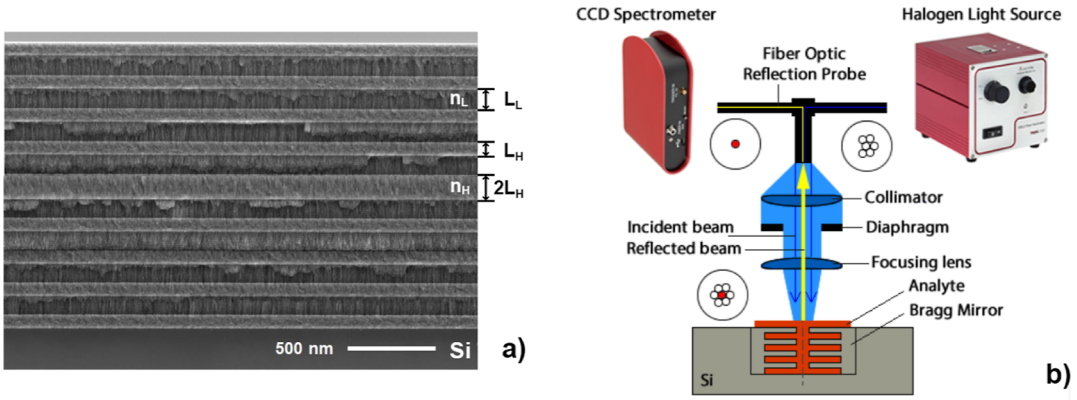

Figure 8. a) Scanning electron microscopy photo of DBR profile (λ_c = 722 nm, $N_{bilayer}$ = 4, [n_L n_H] = [1.65 2.55]) and (b) experimental setup for measuring samples' reflectance spectra using a reflection probe and CCD-based spectrometer (Thorlabs CCS200).

Table 3. Microcavity Width L_c

		$N_{bilayer}$ = 4		
		[n_L n_H] = [1.65 2.12]	[n_L n_H] = [1.65 2.55]	[n_L n_H] = [2.12 2.55]
		L_c, nm	L_c, nm	L_c, nm
λ_c, nm	622	148	122	123
λ_c, nm	722	170	140	141
λ_c, nm	822	194	160	162

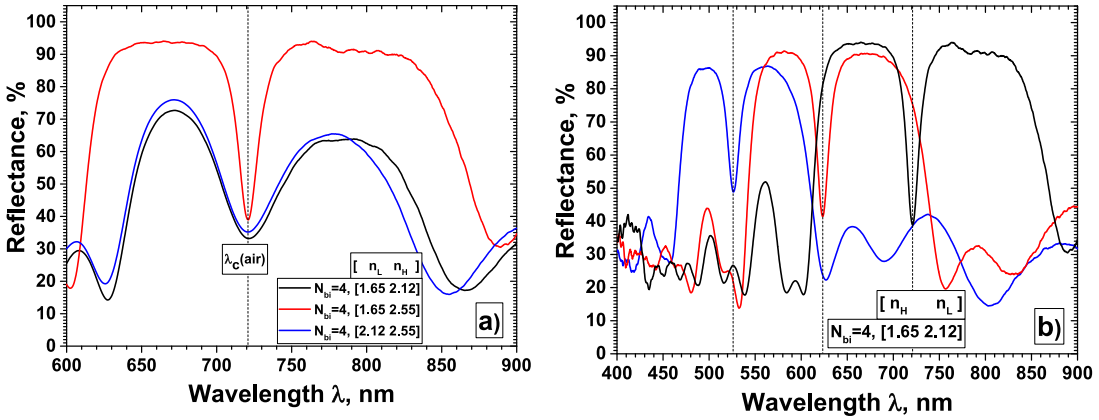

Figure 9. Experimental reflectance spectra for (a) microcavities with [n_L n_H] refractive indexes sets [1.65 2.12], [1.65 2.55], and [2.12 2.55] and $N_{bilayer}$ = 4, λ_c = 722 nm and (b) DBRs with λ_c = 522, 622, and 722 nm and N_{bi} = 4, [n_L n_H] = [1.65 2.55].

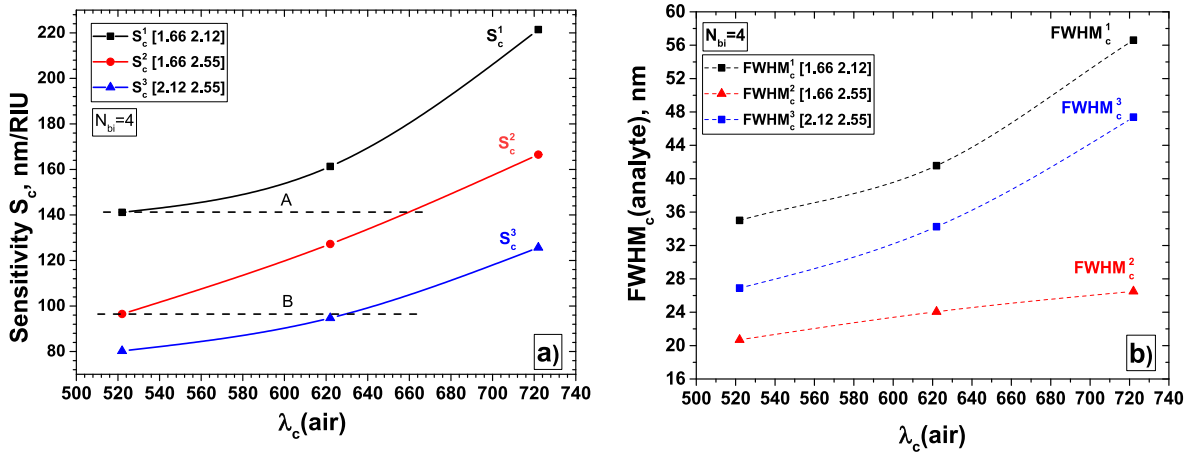

Figure 10. Dependence of microcavity sensitivity S_c (a) and fwhm$_c$(analyte) (b) on λ_c(air) for sets [n_L n_H]: [1.65 2.12], [1.65 2.55], and [2.12 2.55].

https://doi.org/10.1021/acsomega.3c02526
ACS Omega 2023, 8, 21265−21276

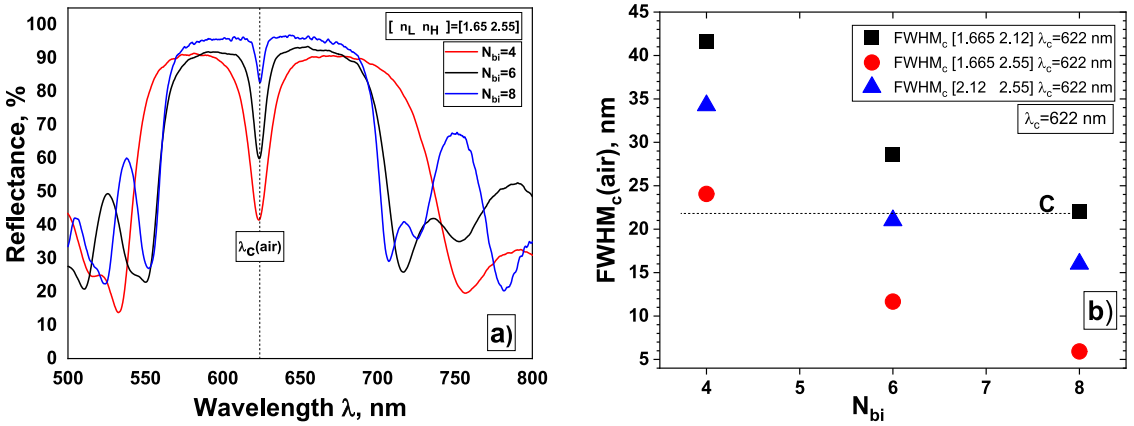

Figure 11. (a) Experimental reflectance spectra of microcavities with $[n_L\ n_H]$ = [1.65 2.55] for $N_{bilayer}$ = 4, 6, 8 and λ_c(air) = 622 nm and (b) dependence of fwhm$_c$ (air) on $N_{bilayer}$ for structures with set $[n_L\ n_H]$: [1.65 2.12], [1.65 2.55], [2.12 2.55].

Eppendorf pipette dispenser. The complete restoration of sensor spectral characteristics after full desorption of analyte from pores was controlled and verified with the CCD-spectrometer. An additional nitrogen purge was used to clean the pores from possible analyte residues before subsequent measurements.

4. EXPERIMENTAL RESULTS AND DISCUSSION

The dependence of reflectance spectra R_c on the wavelength of microcavities with diverse refractive indexes $n_H - n_L$ layer differences, and distinct absolute values of $[n_L\ n_H]$ is depicted in Figure 9a. The other parameters of the structures were identical: $N_{bilayer}$ = 4, λ_c(air) = 722 nm. The dependences of reflectance spectra R_c on cavity mode position λ_c(air) for pores filled with air is detailed in Figure 9b for DBRs with $[n_L$ = 1.65 n_H = 2.12]. The dependences of the microresonator sensitivity S_c and fwhm$_c$ on $[n_L\ n_H]$ and λ_c(air) are displayed in Figure 10a,b, respectively, for $N_{bilayer}$ = 4. The sensitivity S_c increases for microcavities designed at longer wavelengths: $S_c(\lambda_c(\text{air}) = 722\text{ nm}))/S_c(\lambda_c(\text{air}) = 522\text{ nm})) = 1.57$ for DBRs with $[n_L\ n_H]$ = [1.65 2.12] and $S_c(\lambda_c(\text{air}) = 722\text{ nm}))/S_c(\lambda_c(\text{air}) = 522\text{ nm})) = 1.56$ for microcavities with $[n_L\ n_H]$ = [2.12 2.55]. Sensitivity S_c is higher for DBRs with higher porosity layers and accordingly absolute refractive indexes $[n_L\ n_H]$ and difference $n_H - n_L$ goes to minimum values. DBRs with a larger difference $n_H - n_L$ have higher values of reflectance intensity: $R(\lambda_{BP}^L) \rightarrow 100\%$ and $R(\lambda_{BP}^R) \rightarrow 100\%$ and steeper BP edges. Increasing of $n_H - n_L$ also decreases the fwhm$_c$ (Figure 10b) and improves the detectability of the cavity mode. Decreasing fwhm$_c$ changes the detectable shape and parameters of the cavity mode due to a limitation of the spectral resolution: R_c increases and D_c decreases. The fwhm$_c$ is weakly dependent on λ_c for DBR with a high refractive difference: fwhm$_c^2(\lambda_c = 722\text{ nm}) -$ fwhm$_c^2(\lambda_c = 522\text{ nm}) = 5.8$ nm for DBR with $n_H - n_L = 0.89$ contrary to fwhm$_c$1$(\lambda_c = 722$ nm) − fwhm$_c^1(\lambda_c = 522\text{ nm}) = 40.3$ nm for DBR with $n_H - n_L$ = 0.46. DBRs with the highest experimental refractive index contrast have the minimum fwhm$_c$ regardless of having the maximum sensitivity and λ_c: $S_c^1(\Delta n_{LH} = 0.46)/S_c^2(\Delta n_{LH} = 0.89) = 1.7$ for λ_c = 522 nm.

Experimental reflectance spectra of microcavities with a number of bilayers $N_{bilayer}$ = 4, 6, 8 is depicted in Figure 11a (λ_c = 622 nm, $[n_L\ n_H]$ = [1.65 2.55]). The dependence of the fwhm$_c$ on the number of bilayers N_{bi} is illustrated in Figure 11b for λ_c = 622 nm and sets $[n_L\ n_H]$: [1.65 2.12], [1.65 2.55], and [2.12 2.55]. The fwhm$_c$ is smaller for DBRs with a larger number of $N_{bilayer}$ for any sets of refractive index: fwhm$_c(N_{bi}$ = 4) > fwhm$_c(N_{bi}$ = 6) > fwhm$_c(N_{bi}$ = 8). For the microresonator with the largest refractive index contrast ($[n_L\ n_H]$ = [1.65 2.55]) Δfwhm$_c$ = fwhm$_c(N_{bi}$ = 4) − fwhm$_c(N_{bi}$ = 8) = 18.1 nm. The fwhm$_c$ is also smaller and the determination of the cavity mode position is less accurate. On the contrary, the sensitivity S_c is improved for structures with high porosity layers $[n_L \rightarrow n_{air}\ n_H \rightarrow n_{air}]$ and lower refractive index contrast. The precision in the determination of fwhm$_c$ depends on the spectral resolution of the detection device, the integration time, and the noisiness of the spectrum. Also, the reflectance intensity $R(\lambda_{BP})$ increases when the number of bilayers increases (Figure 11a). The dotted line C in Figure 11b indicates that the desired value fwhm$_c$ can be obtained by varying $N_{bilayer}$ or $[n_L\ n_H]$. This allows one to select the appropriate fabricating parameters to tune fwhm$_c$.

4.1. Kinetics of Reflectance Spectra. The kinetics of adsorption/desorption processes of analyte molecules after deposition on the microcavity surface was investigated. The clear signature of the optical mode of the microcavity within the stop-band allowed us to clearly track and determine the shift due to the change of the bilayer effective refractive indexes and induced by adsorption and desorption processes of analyte molecules into/out of pores (Figure 12). The kinetics of reflection spectra in general and the kinetics of the cavity mode position, in particular, are analyte-specific and are dependent

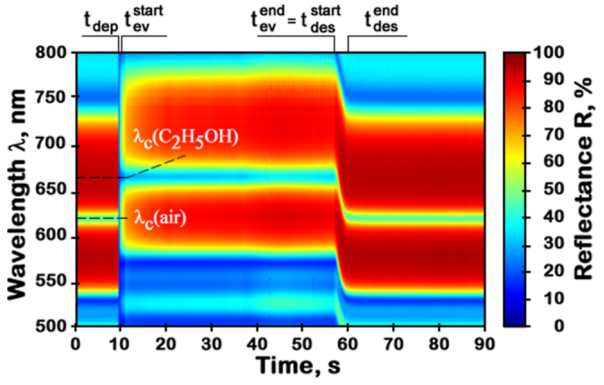

Figure 12. Dependence of reflectance spectra of a microcavity on time after ethanol deposition. Parameters of the structure are λ_c = 622 nm, N_{bi} = 4, $[n_L\ n_H]$ = [1.65 2.55].

https://doi.org/10.1021/acsomega.3c02526
ACS Omega 2023, 8, 21265−21276

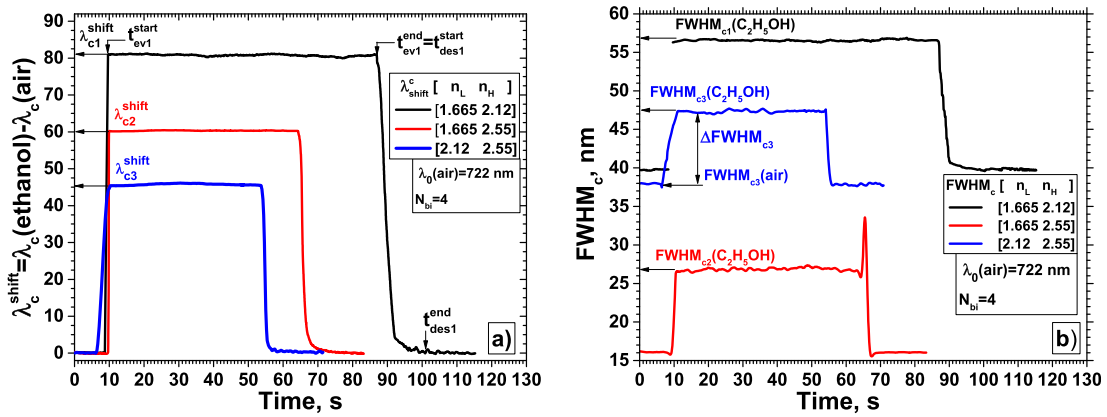

Figure 13. Dependence of the cavity mode position shift λ_c^{shift} (a) and fwhm$_c$ (b) on time after ethanol (96%) deposition on the surface for layer parameters [n_L n_H]: [1.65 2.12], [1.65 2.55], and [2.12 2.55]. Microcavity parameters are λ_c(air) = 722 nm, $N_{bilayer}$ = 4.

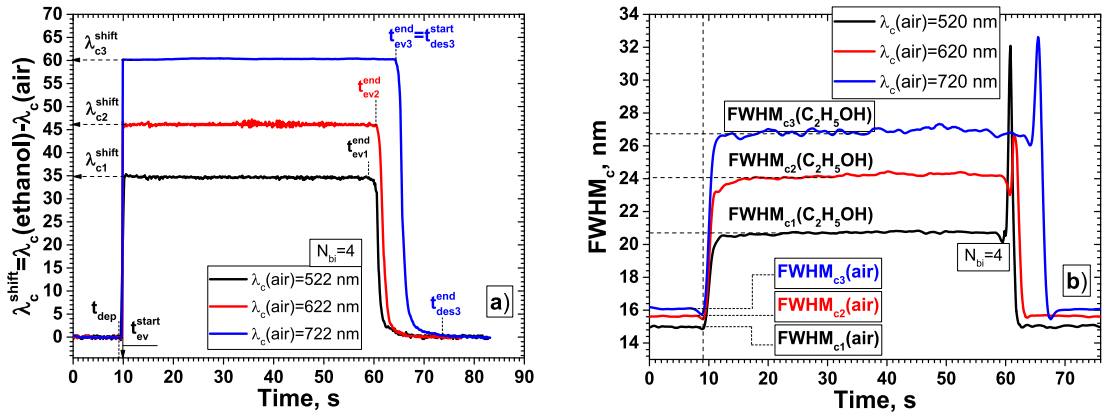

Figure 14. Dependence of cavity mode position shift λ_c^{shift} (a) and fwhm$_c$ (b) on time after ethanol (96%) deposition on the surface for microcavities designed at λ_c = 522, 622, and 722 nm. Sample parameters are $N_{bilayer}$ = 4, [n_L n_H] = [1.65 2.55].

on pore morphology, the interaction of analyte molecules with pores walls and with each other, the properties of the analyte, and capillary effects.[46−48] The typical time dependence of reflectance spectra of a microcavity after ethanol (96%) deposition on the surface at moment t_{dep} is illustrated in Figure 12 (parameters are λ_c = 622 nm, N_{bi} = 4, [n_L n_H] = [1.65 2.55]). The red shift of the cavity mode position is observed from λ_c(air) to $\lambda_c(C_2H_5OH)$ after deposition of the liquid analyte on the sample surface at t_{dep} and completion of the adsorption of the analyte into the pores. The evaporation of the liquid analyte layer from the surface continues from t_{ev}^{start} till t_{ev}^{end}. In this time interval $\lambda_c(C_2H_5OH)$ = const. Desorption of analyte molecules from pores starts at $t_{ev}^{end} = t_{des}^{start}$ and completes at t_{des}^{end}, when $\lambda_c(t_{des}^{end}) \simeq \lambda_c(t_{dep}) = \lambda_c$(air). Due to physical and chemical adsorption of analyte molecules into pore walls and the presence of analyte vapor in pores, $\lambda_c(t_{des}^{end})$ cannot return completely to λ_c(air): $\lambda_c(t_{des}^{end}) \geq \lambda_c$(air). The accuracy in determining the cavity mode position is much better compared to a single DBR due to a smaller dependence of the BP shape on the analyte desorption processes from the pores.

Time dependence of the cavity mode shift $\lambda_c^{shift} = \lambda_c$(ethanol) − λ_c(air) and the fwhm$_c$ after deposition of liquid analyte on the surface for different sets [n_L n_H] are displayed in Figure 13a,b, respectively. The shift λ_c^{shift} (Figure 13a) and the corresponding sensitivity S_c (Figure 10a) are proportional to the total porosity $P_{microcavity}$ ([n_L n_H]) = f([n_L n_H]) of the structure: with $P_{microcavity1}$([1.65 2.12]) > $P_{microcavity2}$([1.65 2.55]) > $P_{microcavity3}$([2.12 2.55]), $S_{c1} > S_{c2} > S_{c3}$. Also, the time of analyte evaporation from the surface of i-microcavity $t_{ev\,i} = t_{ev\,i}^{end} - t_{ev\,i}^{start}$ is proportional to $P_{microcavity}$:$t_{ev1}(P_{microcavity1}) > t_{ev2}(P_{microcavity2}) > t_{ev3}(P_{microcavity3})$. Since the same volume of analyte was deposited on the surface of the microcavities and the thicknesses L_L and L_H (λ_c = const) of the mirror layers were the same, the authors believe that the obtained dependences of t_{ev} on P_{DBR} can be explained by the complex action of parallel processes such as physical adsorption of analyte molecules on pore walls after pore filling, desorption, and re-absorption of analyte molecules from vapor phase. The internal pore area surface covered with analyte molecules is larger for structures with smaller [n_L n_H], and correspondingly time $t_{des} = t_{des\,i} = t_{des\,i}^{end} - t_{des\,i}^{start}$ to escape from pores is larger: $t_{des1}(P_{microcavity1}) > t_{des2}(P_{microcavity2}) > t_{des3}(P_{microcavity3})$. The spectrum does not undergo any distortion within the time range t_{des}^{start}...t_{des}^{end}, and therefore an accurate assessment of its parameters can be done. The observed blue shift of the optical cavity mode (Figures 12 and 13a) is a direct consequence of the uniform decreasing of the effective refractive indexes of each layer n_L and n_H along the pore axis due to polydesorption of the analyte from the pore walls. The results of simulation[49] confirm this mechanism of desorption.

The time dependences of the cavity mode shift $\lambda_c^{shift} = \lambda_c$(ethanol) − λ_c(air) and the fwhm$_c$ after deposition of liquid analyte on the surface for microcavities designed at λ_c = 522, 622, and 722 nm are depicted in Figure 14a,b, respectively. The parameters of the structures are N_{bi} = 4, [n_L n_H] = [1.65 2.55]. The shift λ_c^{shift}, the sensitivity S_c, and the fwhm$_c$ are

https://doi.org/10.1021/acsomega.3c02526
ACS Omega 2023, 8, 21265−21276

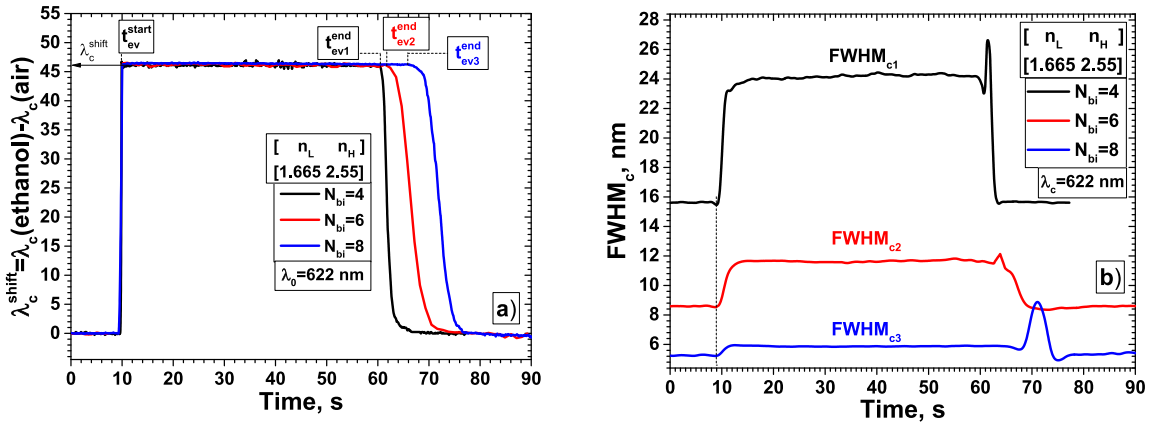

Figure 15. Dependence of cavity mode position shift λ_c^{shift} (a) and fwhm$_c$ (b) on time after ethanol (96%) deposition on the surface for structures with $N_{bilayer}$ = 4, 6, and 8; λ_c = 522, 622, and 722 nm. Sample parameters are λ_c = 622 nm, [n_L n_H] = [1.65 2.55].

proportional to λ_c(air). The time of desorption of analyte molecules from pores is proportional to λ_c due to an increase of the total volume of the pores: $t_{des1}(\lambda_c = 722\ nm) > t_{des2}(\lambda_c = 622\ nm) > t_{des3}(\lambda_c = 522\ nm)$. Microcavities designed at longer wavelength display an increased recovery time but also a longer desorption process time. The time dependence of the cavity mode position on desorption can be exploited as an additional sensor parameter to discriminate analytes.

The time dependences of cavity mode shift $\lambda_c^{shift} = \lambda_c(ethanol) - \lambda_c(air)$ and fwhm$_c$ after deposition of liquid analyte on the surface for microcavities with N_{bi} = 4, 6, and 8 are depicted in Figure 15a,b, respectively. The other parameters of the sensors are the same: λ_c = 622 nm, [n_L n_H] = [1.65 2.55]. Increasing the number of bilayers increases the total internal volume of pores and as a result the desorption time of analyte molecules from pores: $t_{des3}(N_{bi} = 8) > t_{des2}(N_{bi} = 6) > t_{des1}(N_{bi} = 4)$. DBRs with larger number of N_{bi} have smaller fwhm$_c$(air) and Δfwhm$_c$ = fwhm$_c$(analyte) − fwhm$_c$(air): $fwhm_{c3}(N_{bi} = 8) < fwhm_{c1}(N_{bi} = 4)$ and $\Delta fwhm_{c3}(N_{bi} = 8) < \Delta fwhm_{c1}(N_{bi} = 4)$. The sensitivity of S_c does not depend on N_{bi}.

5. CONCLUSIONS

Reflectance spectra of porous Si-based microcavities were computed by the transfer matrix method for all sets [n_L n_H] of bilayer refractive indexes [$1.3 \leq n_L < n_H \leq 1.4$], for structures designed at λ_c = 400...800 nm, and for DBRs with number of bilayers N_{bi} = 3...8. The dependence of sensing parameters as cavity position λ_c, sensitivity S_c, fwhm$_c$, $R_c(\lambda_c)$, $D_c(\lambda_c)$, and fwhm$_{BP}$ on parameters of the optical sensing structure before and after adsorption of analyte molecules into pores were obtained and analyzed. The sensitivity S_c and the fwhm$_c$ of the microcavity are larger for structures with higher absolute values of porosity and accordingly with lower refractive indexes of bilayers (λ_c = 722 nm): $S_c([n_L\ n_H] = [1.65\ 2.12])/S_c([n_L\ n_H] = [2.1\ 2.3]) = 1.76$, $fwhm_c([n_L\ n_H] = [1.65\ 2.12])/fwhm_c([n_L\ n_H] = [2.1\ 2.3]) = 2.13$. The sensitivity S_c is also higher for structures with initial λ_c(air) at longer wavelength regions: $S_c(\lambda_c(air) = 722\ nm))/S_c(\lambda_c(air) = 522\ nm)) = 1.57$ for the optical sensing device with [n_L n_H] = [1.65 2.12]. The fwhm$_c$ decreases with the increase of N_{bi} and can be tuned to improve the detectability of the cavity position λ_c without impacting S_c $fwhm_c$ $(N_{bi} = 8)/fwhm_c(N_{bi} = 4) = 0.53$ for [n_L n_H] = [1.65 2.12]. The kinetics of adsorption/desorption processes of pure ethanol were experimentally investigated for different DBR sets [n_L n_H], λ_c, and N_{bi}. The sensor relaxation time is shorter for structures with a lower total volume of pores and with a shorter bilayer thickness, a lower number of bilayers, and a higher refractive index contrast of bilayers.

AUTHOR INFORMATION

Corresponding Author

Ivan Ivanov − *Taras Shevchenko National University of Kyiv, Kyiv 01033, Ukraine;* orcid.org/0000-0002-8200-5862; Email: ivancko@gmail.com

Authors

Valeriy Skryshevsky − *Taras Shevchenko National University of Kyiv, Kyiv 01033, Ukraine*

Ali Belarouci − *Univ Lyon, ECL, INSA Lyon, CNRS, UCBL, CPE Lyon, INL, UMR5270, Ecully 69130, France*

Complete contact information is available at: https://pubs.acs.org/10.1021/acsomega.3c02526

Author Contributions

I.I., V.S., and A.B. designed the concept and analysis. I.I. and V.S. were involved in experiments and conducted simulations. A.B. fabricated the samples. All authors conducted data processing and wrote the main manuscript. All authors read and approved the final manuscript.

Notes

The authors declare no competing financial interest.

Consent for Publication: the Authors hereby consent to publication of the Work in any and all Springer publications. The Authors warrant that the Work has not been published before in any form.

The datasets obtained during and/or analyzed during the current study are available from the corresponding author on reasonable request.

ACKNOWLEDGMENTS

This work was partially supported by the ANR, France project "Hotline" ANR-19-CE09-0003. This work was partially supported by the EU Horizon 2020 Research and Innovation Staff Exchange Programme (RISE) under the Marie Skłodowska-Curie Action (project 101008159 "UNAT") and the Ministry of Education and Science of Ukraine.

https://doi.org/10.1021/acsomega.3c02526
ACS Omega 2023, 8, 21265−21276

REFERENCES

(1) Porous silicon optical devices for sensing applications. In *Porous silicon: from formation to application*; Korotcenkov, G., Ed.;CRC Press: USA, 2016.

(2) Canham, L. *Handbook of Porous Silicon*; Springer International Publishing, 2014.

(3) Torres-Costa, V.; Agulló-Rueda, F.; Martín-Palma, R. J.; Martínez-Duart, J. M. Porous silicon optical devices for sensing applications. *Opt. Mater.* **2005**, *27*, 1084−1087.

(4) Sailor, M. J. *Porous Silicon in Practice: Preparation, Characterization and Applications*; Wiley-VCH, 2012.

(5) Anto Pradeep, J.; Gogoi, P.; Agarwal, P. Single and multilayer porous silicon structures for photonic applications. *J. Non-Cryst. Solids* **2008**, *354*, 2544−2547.

(6) Galeazzo, E.; Peres, H. E. M.; Santos, G.; Peixoto, N.; Ramirez-Fernandez, F. J. Gas sensitive porous silicon devices: responses to organic vapors. *Sens. Actuators, B* **2003**, *93*, 384−390.

(7) Stefano, L. D.; Rotiroti, L.; Rea, I.; Moretti, L.; Francia, G. D.; Massera, E.; Lamberti, A.; Arcari, P.; Sanges, C.; Rendina, I. Porous silicon-based optical biochips. *J. Opt. A: Pure Appl. Opt.* **2006**, *8*, S540−S544.

(8) Snow, P. A.; Squire, E. K.; Russell, P. S. J.; Canham, L. T. Vapor sensing using the optical properties of porous silicon Bragg mirrors. *J. Appl. Phys.* **1999**, *86*, 1781−1784.

(9) Huanca, D. R.; Ramirez-Fernandez, F. J.; Salcedo, W. J. Porous silicon optical cavity structure applied to high sensitivity organic solvent sensor. *Microelectron. J.* **2008**, *39*, 499−506.

(10) Rodriguez, G. A.; Ryckman, J. D.; Jiao, Y.; Weiss, S. M. A size selective porous silicon grating-coupled Bloch surface and sub-surface wave biosensor. *Biosens. Bioelectron.* **2014**, *53*, 486−493.

(11) Guillermain, E.; Lysenko, V.; Orobtchouk, R.; Benyattou, T.; Roux, S.; Pillonnet, A.; Perriat, P. Bragg surface wave device based on porous silicon and its application for sensing. *Appl. Phys. Lett.* **2007**, *90*, 241116.

(12) Joannopoulos, J. D.; Johnson, S. G.; Winn, J. N.; Meade, R. D. *Photonic Crystals*; Princeton University Press, 2008.

(13) Bruyant, A.; Lérondel, G.; Reece, P. J.; Gal, M. All-silicon omnidirectional mirrors based on one-dimensional photonic crystals. *Appl. Phys. Lett.* **2003**, *82*, 3227−3229.

(14) Sánchez-Sobrado, O.; Lozano, G.; Calvo, M. E.; Sánchez-Iglesias, A.; Liz-Marzán, L. M.; Míguez, H. Interplay of Resonant Cavity Modes with Localized Surface Plasmons: Optical Absorption Properties of Bragg Stacks Integrating Gold Nanoparticles. *Adv. Mater.* **2011**, *23*, 2108−2112.

(15) Frascella, F.; Ricciardi, S.; Rivolo, P.; Moi, V.; Giorgis, F.; Descrovi, E.; Michelotti, F.; Munzert, P.; Danz, N.; Napione, L.; Alvaro, M.; Bussolino, F. A Fluorescent One-Dimensional Photonic Crystal for Label-Free Biosensing Based on Bloch Surface Waves. *Sensors* **2013**, *13*, 2011−2022.

(16) Lee, S. H.; Ha, N. Y. Sol−Gel Substrates with Engineered Multiple Photonic Bandgaps for Full-Color Photonic Devices. *Small* **2011**, *7*, 2704−2708.

(17) Piya, R.; Gupta, B.; Gooding, J. J.; Reece, P. J. Optimising porous silicon Bragg reflectors for narrow spectral resonances. *J. Appl. Phys.* **2018**, *124*, 163103.

(18) Ivanov, I. I.; Skryshevsky, V. A.; Serdiuk, T.; Lysenko, V. Kinetics of adsorption-desorption processes of alcohol molecules in porous silicon Bragg mirror. *Sens. Actuators, B* **2012**, *174*, 521−526.

(19) Pavesi, L.; Mazzoleni, C.; Tredicucci, A.; Pellegrini, V. Controlled photon emission in porous silicon microcavities. *Appl. Phys. Lett.* **1995**, *67*, 3280−3282.

(20) Sciacca, B.; Frascella, F.; Venturello, A.; Rivolo, P.; Descrovi, E.; Giorgis, F.; Geobaldo, F. Doubly resonant porous silicon microcavities for enhanced detection of fluorescent organic molecules. *Sens. Actuators, B* **2009**, *137*, 467−470.

(21) Jenie, S. N. A.; Prieto-Simon, B.; Voelcker, N. H. Development of l-lactate dehydrogenase biosensor based on porous silicon resonant microcavities as fluorescence enhancers. *Biosens. Bioelectron.* **2015**, *74*, 637−643.

(22) Lorenzo, E.; Oton, C. J.; Capuj, N. E.; Ghulinyan, M.; Navarro-Urrios, D.; Gaburro, Z.; Pavesi, L. Porous silicon-based rugate filters. *Appl. Opt.* **2005**, *44*, 5415−5421.

(23) Ge, D.; Shi, J.; Wei, J.; Zhang, L.; Zhang, Z. Optical sensing analysis of bilayer porous silicon nanostructure. *J. Phys. Chem. Solids* **2019**, *130*, 217−221.

(24) León, X.; Gennaro, A. M.; Rodi, P. M.; Forzani, L.; Pacio, M.; Juárez, H.; Osorio, E.; Koropecki, R. R. Formation of lipid bilayers on the pore walls of macroporous silicon. *Thin Solid Films* **2019**, *672*, 120−125.

(25) Ramakrishan, S. K.; Martin Fernandez, M.; Cloitre, T.; Agarwal, V.; Cuisinier, F. J. G.; Gergely, C. Porous silicon microcavities redefine colorimetric ELISA sensitivity for ultrasensitive detection of autoimmune antibodies. *Sens. Actuators, B* **2018**, *272*, 211−218.

(26) Palestino, G.; Legros, R.; Agarwal, V.; Pérez, E.; Gergely, C. Functionalization of nanostructured porous silicon microcavities for glucose oxidase detection. *Sens. Actuators, B* **2008**, *135*, 27−34.

(27) Hiraoui, M.; Guendouz, M.; Lorrain, N.; Moadhen, A.; Haji, L.; Oueslati, M. Spectroscopy studies of functionalized oxidized porous silicon surface for biosensing applications. *Mater. Chem. Phys.* **2011**, *128*, 151−156.

(28) Lasave, L. C.; Urteaga, R.; Koropecki, R. R.; Gonzalez, V. D.; Arce, R. D. Real-time study of protein adsorption kinetics in porous silicon. *Colloids Surf., B* **2013**, *111*, 354−359.

(29) Oliinyk, B. V.; Isaieva, K.; Manilov, A. I.; Nychyporuk, T.; Geloen, A.; Joffre, F.; Skryshevsky, V. A.; Litvinenko, S. V.; Lysenko, V. Silicon-Based Optoelectronic Tongue for Label-Free and Non-specific Recognition of Vegetable Oils. *ACS Omega* **2020**, *5*, 5638−5642.

(30) Wilson, A. D. Review of Electronic-nose Technologies and Algorithms to Detect Hazardous Chemicals in the Environment. *Proc. Technol.* **2012**, *1*, 453−463.

(31) Korotcenkov, G.; Rusu, E. How to Improve the Performance of Porous Silicon-Based Gas and Vapor Sensors? Approaches and Achievements. *Phys. Status Solidi* **2019**, *216*, 1900348.

(32) Di Natale, C.; Paolesse, R.; Macagnano, A.; Mantini, A.; D'Amico, A.; Legin, A.; Lvova, L.; Rudnitskaya, A.; Vlasov, Y. Electronic nose and electronic tongue integration for improved classification of clinical and food samples. *Sens. Actuators, B* **2000**, *64*, 15−21.

(33) Zaragozá, P.; Fernández-Segovia, I.; Fuentes, A.; Vivancos, J. L.; Ros-Lis, J. V.; Barat, J. M.; Martínez-Máñez, R. Monitorization of Atlantic salmon (Salmo salar) spoilage using an optoelectronic nose. *Sens. Actuators, B* **2014**, *195*, 478−485.

(34) Létant, S. E.; Content, S.; Tan, T. T.; Zenhausern, F.; Sailor, M. J. Integration of porous silicon chips in an electronic artificial nose. *Sens. Actuators, B* **2000**, *69*, 193−198.

(35) Gongalsky, M. B.; Tsurikova, U. A.; Samsonova, J. V.; Gvindzhiliiia, G. Z.; Gonchar, K. A.; Saushkin, N. Y.; Kudryavtsev, A. A.; Kropotkina, E. A.; Gambaryan, A. S.; Osminkina, L. A. Double etched porous silicon nanowire arrays for impedance sensing of influenza viruses. *Results Mater.* **2020**, *6*, 100084.

(36) Park, S. H.; Lee, K. W.; Kim, Y. Y. A technique for the fabrication of various multiparametric porous silicon samples on a single substrate. *Thin Solid Films* **2010**, *518*, 2860−2863.

(37) del Valle, M. Sensor Arrays and Electronic Tongue Systems. *Int. J. Electrochem.* **2012**, *2012*, 1−11.

(38) Zhang, J.; Xue, Y.; Sun, Q.; Zhang, T.; Chen, Y.; Yu, W.; Xiong, Y.; Wei, X.; Yu, G.; Wan, H.; Wang, P. A miniaturized electronic nose with artificial neural network for anti-interference detection of mixed indoor hazardous gases. *Sens. Actuators, B* **2021**, *326*, 128822.

(39) Fathi, F.; Rashidi, M. R.; Pakchin, P. S.; Ahmadi-Kandjani, S.; Nikniazi, A. Photonic crystal based biosensors: Emerging inverse opals for biomarker detection. *Talanta* **2021**, *221*, 121615.

(40) Mohankumar, P.; Ajayan, J.; Mohanraj, T.; Yasodharan, R. Recent developments in biosensors for healthcare and biomedical applications: A review. *Measurement* **2021**, *167*, 108293.

https://doi.org/10.1021/acsomega.3c02526
ACS Omega 2023, 8, 21265−21276

(41) Jung, Y.; Huh, Y.; Kim, D. Recent advances in surface engineering of porous silicon nanomaterials for biomedical applications. *Microporous Mesoporous Mater.* **2021**, *310*, 110673.
(42) Jabbar, A. A.; Alwan, A. M.; Zayer, M. Q.; Bohan, A. J. Efficient single cell monitoring of pathogenic bacteria using bimetallic nanostructures embedded in gradient porous silicon. *Mater. Chem. Phys.* **2020**, *241*, 122359.
(43) Guermit, N.; Remache, L.; Lorrain, N.; Guendouz, M.; Charrier, J. Theoretical and experimental study of Fermi Bragg reflector as application for thin silicon solar cells. *Opt. Mater.* **2020**, *100*, 109615.
(44) Mackay, T. G.; Lakhtakia, A. The Transfer-Matrix Method in Electromagnetics and Optics. *Synth. Lect. Comput. Electromagn.* **2020**, *1*, 1−126.
(45) Ivanov, I. I.; Skryshevsky, V. A.; Belarouci, A. Porous Bragg reflector based sensors: Ways to increase sensitivity. *Sens. Actuators, A* **2020**, *315*, 112234.
(46) Kayahan, E.; Bahsi, Z. B.; Oral, A. Y.; Sezer, M. Porous silicon based sensor for organic vapors. *Acta Phys. Pol., A* **2015**, *127*, 1400−1402.
(47) Gole, J. L.; Lewis, S. E. Nanostructure and morphology modified porous silicon sensors. *Quantum Sens. Nanophotonic Devices II* **2005**, *5732*, 573.
(48) De Stefano, L.; Rendina, I.; Moretti, L.; Tundo, S.; Rossi, A. M. Smart optical sensors for chemical substances based on porous silicon technology. *Appl. Opt.* **2004**, *43*, 167−172.
(49) Ivanov, I. I.; Skryshevsky, V. A.; Belarouci, A. Chemical sensor based on the colorimetric response of porous silicon photonic crystal. *Sens. Actuators, A* **2022**, *333*, 113309.

https://doi.org/10.1021/acsomega.3c02526
ACS Omega 2023, 8, 21265−21276